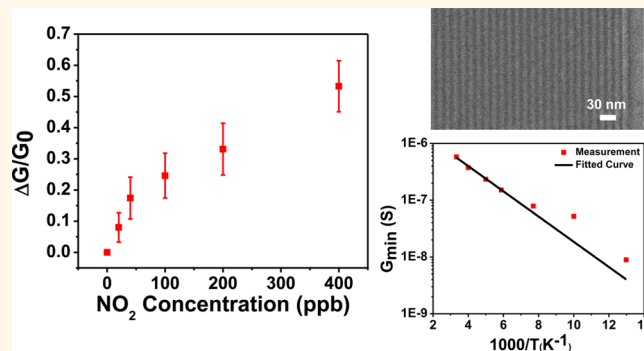


# Patterning, Characterization, and Chemical Sensing Applications of Graphene Nanoribbon Arrays Down to 5 nm Using Helium Ion Beam Lithography

Ahmad N. Abbas,<sup>†,§</sup> Gang Liu,<sup>†</sup> Bilu Liu,<sup>†</sup> Luyao Zhang,<sup>†</sup> He Liu,<sup>†</sup> Douglas Ohlberg,<sup>‡</sup> Wei Wu,<sup>†</sup> and Chongwu Zhou<sup>†,\*</sup>

<sup>†</sup>Department of Electrical Engineering, University of Southern California, Los Angeles, California 90089, United States, <sup>‡</sup>Intelligent Infrastructure Lab, HP Laboratories, Hewlett-Packard Co., Palo Alto, California 94304, United States, and <sup>§</sup>Department of Electrical Engineering, King Abdulaziz University, Abdullah Sulayman Street, Jeddah 22254, Saudi Arabia

**ABSTRACT** Bandgap engineering of graphene is an essential step toward employing graphene in electronic and sensing applications. Recently, graphene nanoribbons (GNRs) were used to create a bandgap in graphene and function as a semiconducting switch. Although GNRs with widths of <10 nm have been achieved, problems like GNR alignment, width control, uniformity, high aspect ratios, and edge roughness must be resolved in order to introduce GNRs as a robust alternative technology. Here we report patterning, characterization, and superior chemical sensing of ultranarrow aligned GNR arrays down to 5 nm width using helium ion beam lithography (HIBL) for the first time. The patterned GNR arrays possess narrow and adjustable widths, high aspect ratios, and relatively high quality. Field-effect transistors were fabricated on such GNR arrays and temperature-dependent transport measurements show the thermally activated carrier transport in the GNR array structure. Furthermore, we have demonstrated exceptional NO<sub>2</sub> gas sensitivity of the 5 nm GNR array devices down to parts per billion (ppb) levels. The results show the potential of HIBL fabricated GNRs for the electronic and sensing applications.



**KEYWORDS:** graphene nanoribbon · array · helium ion beam lithography · field-effect transistor

Since the rise of graphene, it has attracted strong attention due to its exceptional electronic,<sup>1</sup> thermal,<sup>2,3</sup> mechanical,<sup>4,5</sup> and optical properties.<sup>6–8</sup> Due to the lack of an energy bandgap in graphene, electronic applications of graphene have been limited to functionalities where switching off the device is not necessary. Accordingly, technologies such as graphene radio frequency transistors have been drawing lots of attention because it is easily implementable in real life applications.<sup>9–11</sup> On the contrary, digital electronics applications require a sufficient bandgap for the channel material in order to switch off the device for proper operation. As a result, extensive research was done to

use graphene as a digital switch by employing novel device structures that made use of the high tunability of graphene Fermi level.<sup>12–16</sup> Although these devices perform fairly well, their structures are complex and lack the use of excellent charge transport properties of graphene. On the other hand, numerous efforts were devoted to induce a bandgap in graphene by chemical modification,<sup>17–19</sup> use of multilayer graphene with dual gates,<sup>20–22</sup> and other methods.<sup>23</sup> Nevertheless, these methods are either difficult to control or devices fail to perform well.

Recently, the narrowing of graphene into stripes with widths ~10 nm was studied both theoretically<sup>24</sup> and experimentally<sup>25</sup> to

\* Address correspondence to chongwuz@usc.edu.

Received for review November 5, 2013 and accepted January 23, 2014.

Published online 10.1021/nn405759v

© XXXX American Chemical Society

create an energy bandgap in the electronic structure of graphene due to quantum confinement. However, the theoretical predictions and the experimental data did not match due to inability to control edge structures and edge states of graphene which contribute to the creation of a transport gap.<sup>26</sup> Consequently, several methods were used to create GNRs including top down etching of graphene into GNR,<sup>25,27,28</sup> unzipping of carbon nanotubes,<sup>29–33</sup> chemically producing GNR,<sup>34–36</sup> bottom-up chemical synthesis,<sup>37–39</sup> and various methods for producing arrays of GNR.<sup>33,40–45</sup> Additionally, several interesting transport properties were experimentally tested for several types of GNRs.<sup>46,47</sup> Nevertheless, in order to create a reliable technology that uses GNR as a platform, better control of GNR should be accomplished. And issues like GNR alignment, width control, aspect ratios, ribbon to ribbon variations, density of GNR and the quality of the materials have to be precisely and reproducibly controlled. These features are essential to control the electronic characteristics of the devices fabricated and proper operation of complex circuits.

Helium ion beam lithography (HIBL)<sup>48,49</sup> and helium ion microscopy<sup>50</sup> have recently demonstrated high resolutions mainly due to their small beam spot size and relatively small scattering length.<sup>51</sup> Additionally, it has been recently shown that HIBL can cut and pattern graphene with features down to  $\sim 10$  nm.<sup>52,53</sup> Furthermore, HIBL was used to create random defects in a graphene lattice in order to open a bandgap.<sup>23</sup> Nevertheless, those techniques did not take advantage of the extremely high resolution and control HIBL can offer. Here we report the use of HIBL to create GNR field-effect transistors (GNR FETs) with highly dense GNR arrays with one of the smallest half-pitch GNR reported to date. In addition, we can control the aspect ratio of the GNR up to 400 (*i.e.*, the widths and lengths of GNRs are 5 and 2000 nm, respectively). Raman spectra of HIBL fabricated GNRs show relatively large G-band to D-band intensity ratios (*i.e.*,  $I_G/I_D$ ) which indicate the quality of these GNRs compared to lithographically etched GNRs.<sup>54</sup> Subsequently, we have performed low temperature electrical measurements of the 5 nm GNR array device and observed thermal activation behavior of carriers in the graphene/GNR junction. Finally, we measured the sensitivity of GNR arrays to NO<sub>2</sub> gas and observed parts per billion (ppb) level sensitivity showing the potential for using HIBL GNR arrays for sensing applications.<sup>55–57</sup>

## RESULTS AND DISCUSSIONS

Figure 1a shows the fabrication steps for the HIBL GNR array transistors. First, chemical vapor deposition (CVD) graphene was transferred onto a P<sup>2+</sup> Si/SiO<sub>2</sub> wafer using common polymer-mediated transfer techniques.<sup>4,58,59</sup> Then, Ti/Au electrodes were patterned on top of graphene to form contacts for source and

drain. Afterward, a channel definition took place using oxygen reactive ion etch (RIE) to remove unwanted graphene. Finally, the whole device was loaded into a HIBL machine to create the desired GNR patterns. Figure 1b–d shows helium ion microscope images of several GNR half-pitches (*i.e.*, 5, 6, and 7.5 nm, respectively). These images show the precise control of the widths, spacing, as well as the alignment of GNRs we achieved for GNR arrays (*i.e.*, the bright lines in the helium ion microscope image is graphene). Additionally, Figure 1e shows the high aspect ratios and density we can achieve using HIBL. For the employed device structure, the Ti/Au electrodes contact graphene which makes graphene the actual source and drain in contact with the GNR array channel (Figure 1f). Helium ion microscope was used to capture all the images of the GNR arrays, which cannot otherwise be imaged by scanning electron microscope (SEM), because helium ion microscope not only has better resolution but also better signal to image graphene patterns. The interaction volume of helium ions is much smaller than that of electrons, and thus, the image carries more information from surface properties (*i.e.*, the graphene layer). For all the devices created using HIBL, we have used monolayer graphene CVD (Figure S1).

To assess the quality of HIBL GNRs, Raman spectra of the GNR arrays were performed. Figure 2a shows the Raman spectra of GNR arrays with 5, 6, 8, 10, and 15 nm half-pitch. For all the Raman spectra measurements, a 532 nm laser was used. It can be observed that the G-band ( $\sim 1589$  cm<sup>-1</sup>) and the 2D-band ( $\sim 2670$  cm<sup>-1</sup>) broaden as the widths of GNR decrease from 15 to 5 nm. For GNR with widths of 5 and 6 nm, the 2D-band cannot be distinguished due to further broadening. This can be explained by softening of the phonons because of the dominance of defects in the GNR lattice.<sup>60</sup> Simultaneously, since for narrower GNR the defects represent a higher percentage of the Raman signal, the heterogeneous nature near the edge causes the broadening of the peaks.<sup>54</sup> Moreover, it has been predicted that the G-band upshifts in frequency with decreasing GNR widths which can be explained by the fact that with higher defect densities higher frequency phonons are allowed and an additional peak merges with the G-band peak which results in an apparent upshift in frequency.<sup>60</sup> However, the G-band shift we observed is random and not monotonic (Figure S2). The G-band shift can also be explained by quantum confinement effects in GNR.<sup>61</sup> Figure 2b shows the dependence of  $I_G/I_D$  on the inverse of GNR array half-pitch (*i.e.*, GNR width). This plot shows the effect of increasing the percentage of edge defects on both G- and D-bands. Below a certain size, the number of ordered carbon rings compared to defects decrease and  $I_D$  decreases accordingly. On the other hand,  $I_G$  is related to the bond stretching of sp<sup>2</sup> bond and accordingly will not be affected by GNR narrowing.<sup>60</sup>

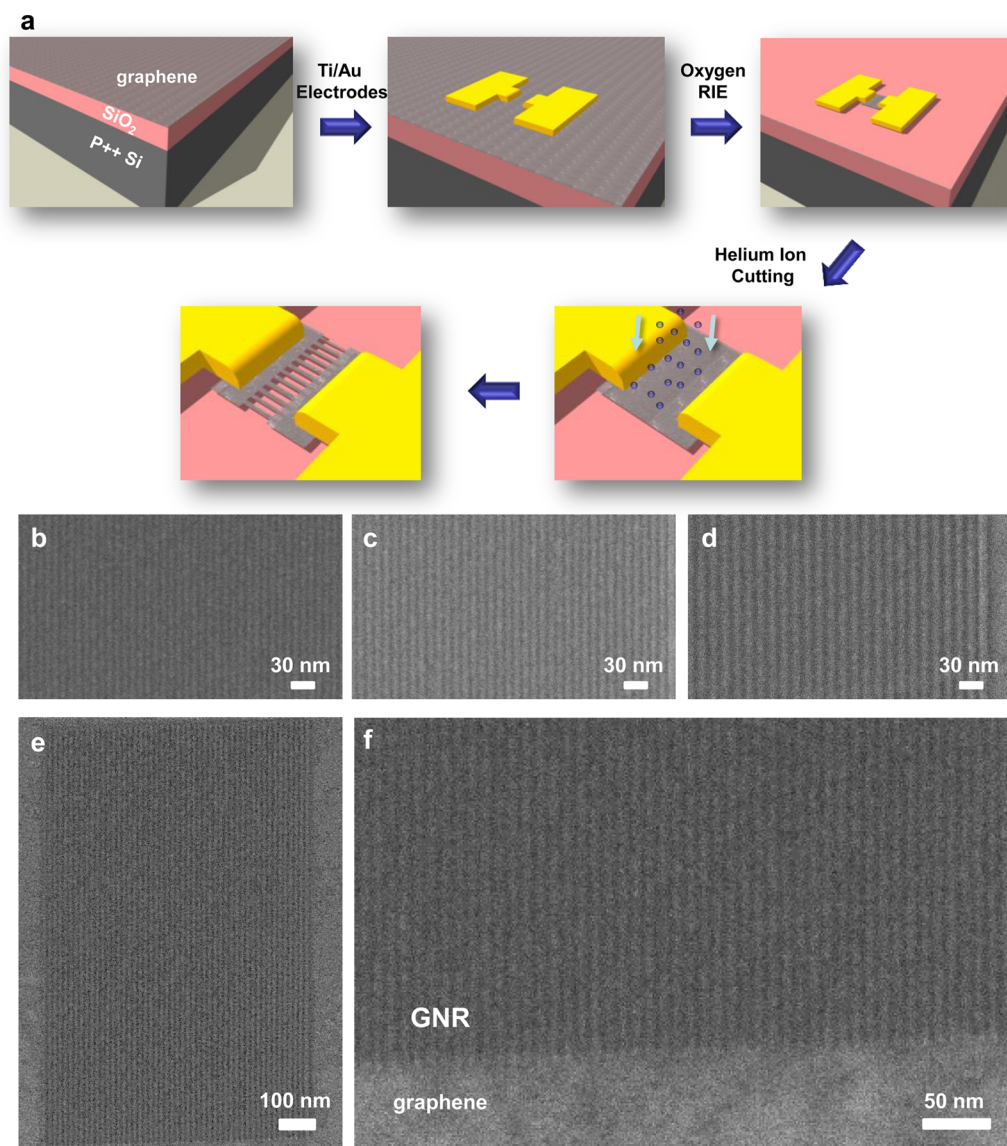


Figure 1. (a) Scheme of GNR arrays fabricated by HIBL. (b–d) Helium ion microscope images of (b) 5 nm, (c) 6 nm, and (d) 7.5 nm half-pitch arrays. (e) Helium ion microscope image of high aspect ratio GNRs (width  $\times$  length is 5 nm  $\times$  1200 nm). (f) Helium ion microscope image shows smooth interface between graphene and patterned GNRs. For all images, bright lines represent graphene.

Consequently, the  $I_G/I_D$  will increase as GNRs get smaller which further confirms Ryu *et al.*'s<sup>54</sup> observation on Raman relaxation length of D-mode phonons. The measured  $I_G/I_D$  data points in Figure 2b can be fitted into a line with equation:  $I_G/I_D \approx 8.39/W$ , where  $W$  is the width of GNRs in nanometers. This equation does not apply to wider GNR (*i.e.*,  $W \geq 15$  nm) because the mechanisms that govern  $I_D$  are different.<sup>54,60,62</sup> Furthermore, comparing  $I_G/I_D$  for the same width can give an indication about the quality of the patterned GNRs. In Figure 2c we compare our  $I_G/I_D$  to other recent publications in order to highlight the relative quality of HIBL GNR patterning. Since  $I_G$  originates from the doubly degenerate zone center mode which corresponds to the carbon atoms ( $sp^2$  bond) phonons in graphene<sup>62</sup> and  $I_D$  corresponds to various defects in

graphene (*e.g.*, vacancies, stone-wales, foreign adatoms and edge defects),<sup>60,63,64</sup> the ratio of  $I_G/I_D$  for the same GNR width can be a measure for material quality. For example, our 15 nm wide GNRs have  $I_G/I_D$  of 0.52 compared to 0.2 for electron beam lithography (EBL) patterned GNR.<sup>54</sup> This highlights the quality of GNRs patterned with HIBL compared to other lithography based techniques.

Electrical measurements were carried out for the GNR array devices using  $P^{2+}$  Si as a back gate. We performed the measurements on a 6 nm half-pitch GNR array device with a long channel length (*i.e.*, 2  $\mu$ m). Figure 3a shows the graphene device before patterning the GNR with a Dirac point close to zero gate voltage. Figure 3b,c shows the device performance after patterning the GNR array devices at 300 and 77 K,

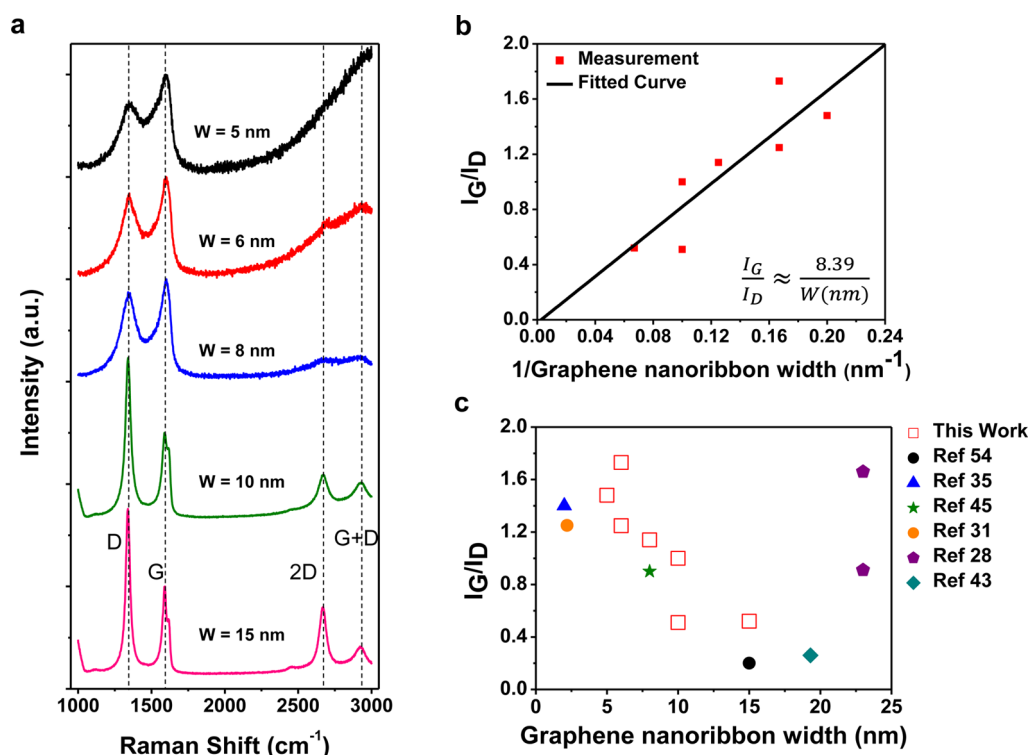


Figure 2. Raman spectra of HIBL patterned GNR arrays. (a) 5, 6, 8, 10, 15 nm half-pitch. (b) G-band ( $I_G$ ) to D-band ( $I_D$ ) intensity ratios versus the inverse of the GNR array half-pitch and the corresponding fitted curve. (c) G-band ( $I_G$ ) to D-band ( $I_D$ ) intensity ratios of this work compared to some recent publications.

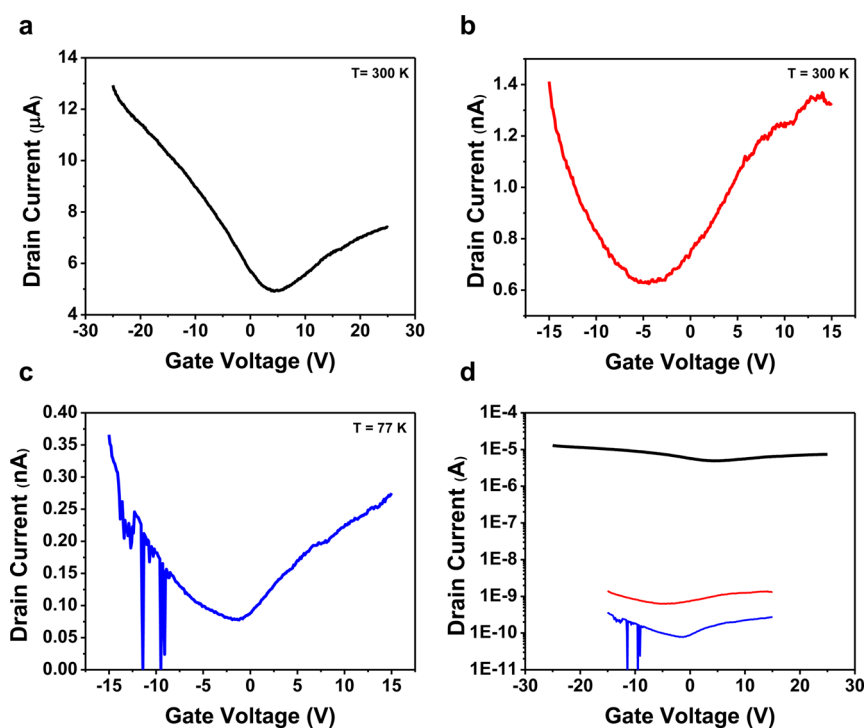


Figure 3. Transfer characteristics of (a) graphene device before patterning, (b) device after patterning 6 nm GNR arrays at room temperature, and (c) 6 nm GNR array device measured at (77 K). (d) Transfer characteristics in log scale of a–c.  $V_d$  was 0.1 V for all the measurements.

respectively. To compare the ON/OFF ratios of the GNR array device at different conditions, we define the ON/OFF ratio to be the current at gate voltage of

( $V_g = -15\text{ V}$ ) divided by the minimum current at the charge neutrality point. It can be observed that the ON/OFF ratio increases from 2 to 2.25 after patterning



the GNR at 300K and reaches a value of 4.75 at 77K. Additionally, the minimum conductance decreased for the device from 300 to 77 K which is a typical semi-conducting behavior. Figure 3d shows all the measured curves under log scale. It should be noted that the ON current level dropped dramatically after patterning the GNR array. Moreover, it should be noted that the gate voltage sweeping range in the GNR array device is smaller than that of the graphene device before patterning the GNR. This is due to the increased leakage through the gate oxide after patterning. Additionally, we also measured HIBL GNR with width of 15 nm, and the transport characteristics (Figure S5a) showed ON current value of 4  $\mu$ A at drain voltage of 0.1 V and gate voltage of  $-25$  V, which would convert to a reduction in current density (*i.e.*, current normalized by width) by a factor of  $\sim 2$  when compared to graphene before HIBL. Comparatively, a reduction in current density of  $\sim 5000$  was observed for 6 nm HIBL GNR which may be attributed to: (i) GNR edge scattering which is inversely proportional to GNR width,<sup>65,66</sup> (ii) increased impurity scattering after HIBL due to helium ions breaking Si–O bonds in SiO<sub>2</sub> dielectric and creating surface defect states, (iii) increased electron and hole masses for narrow GNR<sup>67</sup> and (iv) reduced effective transconductance of HIBL GNR devices because of charge traps created in SiO<sub>2</sub> which contribute to effects such as weak Fermi level pinning and the screening of gate electric field which would also negatively affect the ON/OFF ratio.<sup>68,69</sup>

Current degradation for EBL-patterned GNRs was rarely reported; however, our current degradation for 15 nm HIBL GNR compares favorably with limited data we can estimate from ref 66, which reported a degradation of mobility (and thus current) by a factor of 15 when the GNR width goes from 1000 to 15 nm. We believe the main factor for the significant current degradation of 6 nm GNR is that 6 nm is close to the so-called inactive GNR edge width ( $W_0$ ). The conductance of GNR can be described with a linear fit  $G = \sigma(W - W_0)/L$ , where  $\sigma$  is the GNR sheet conductivity,  $W_0$  is the GNR inactive edge width,  $W$  is the GNR width and  $L$  is the GNR length. The inactive GNR edge width is usually believed to be related to contributions from localized edge states scattering due to GNR edge roughness caused by etching.<sup>25</sup> Figure S5b plots the conductance of HIBL GNRs with widths of 15, 10, and 6 nm vs GNR width, and a fit using the above equation yields  $W_0$  of 5.6 nm, which is comparable to  $W_0$  estimated for EBL-patterned GNRs. Furthermore, Raman characterization (Figure 2c) has revealed a similar  $I_G/I_D$  ratio for HIBL GNR in comparison to EBL patterned ones which confirms similar levels of defects created by HIBL and EBL processes.<sup>54</sup>

To evaluate the effect of helium ions scattering in SiO<sub>2</sub>, we performed a Monte Carlo probabilistic analysis based on the high energy stopping of light ions

using commercial software. This simulation sheds light on the effect of defect states in SiO<sub>2</sub> on the gate control and Fermi level tunability in GNR array devices (Figure S3). Principally, in order to improve the device performance, patterning should be made on graphene before transfer. Alternatively, the whole device can be transferred from the substrate by using an oxide etcher and a polymer scaffold. A possible transfer-free method is based on free-standing suspended GNR channel where the SiO<sub>2</sub> underneath the GNR is etched.<sup>70</sup> This method might have a low yield but would be interesting for scientific study purposes.

To study the carrier transport in the patterned GNR arrays, we performed low temperature output characteristic (*i.e.*,  $I_D - V_d$ ) measurements of a device to study the nature of thermionic activation of carriers through the graphene/GNR junction. For this device, in order to have higher operating currents, GNRs with a width of 5 nm and length of 200 nm were patterned. Figure 4a shows the temperature dependence of the  $I_D - V_d$  curves with clear reduction of the conductance as the temperature is reduced. The nonlinearity of the differential conductance near the zero bias point (*i.e.*,  $V_d = 0$  V) is clearly shown for lower temperatures in Figure 4b. This effect indicates a potential barrier created for carriers transporting through graphene/GNR junction. Moreover, estimation of the activation energy ( $E_A$ ) was carried out using the minimum conductance value for each temperature point. Figure 4c shows that the minimum conductance ( $G_{\min}$ ) points fit with the thermally activated carriers' equation:

$$G_{\min} = G_1 e^{-E_A/k_B T}$$

where  $G_1$  is a constant,  $k_B$  is Boltzmann's constant,  $T$  is the absolute temperature, and  $E_A$  is the activation energy. The curve fitting yielded an  $E_A$  of 44 meV, and based on Figure 3b,c, we note that the Dirac point corresponds to a small negative gate voltage, and device at zero gate voltage shows n-type conduction. The  $E_A$  derived based on output characteristics of the device at zero gate voltage (Figure 4) should correspond to the energy difference between metal Fermi level and GNR conduction band, which should be slightly smaller than the energy difference between metal Fermi level and GNR valence band (as the gate voltage corresponding to the Dirac point is slightly negative). The GNR bandgap ( $E_G$ ) is therefore estimated to be  $>88$  meV. Theoretical tight-binding models suggest that a GNR with 5 nm width will have a bandgap  $\sim 0$  to 0.3 eV depending on the edge structure and number of dimer rows.<sup>24</sup> The value extracted from Figure 4 (*i.e.*,  $E_G \geq 0.088$  eV) falls within the expected theoretical values.

One of the very promising applications of GNR devices is chemical sensing.<sup>71</sup> The reduced charge density caused by their small dimensions and the

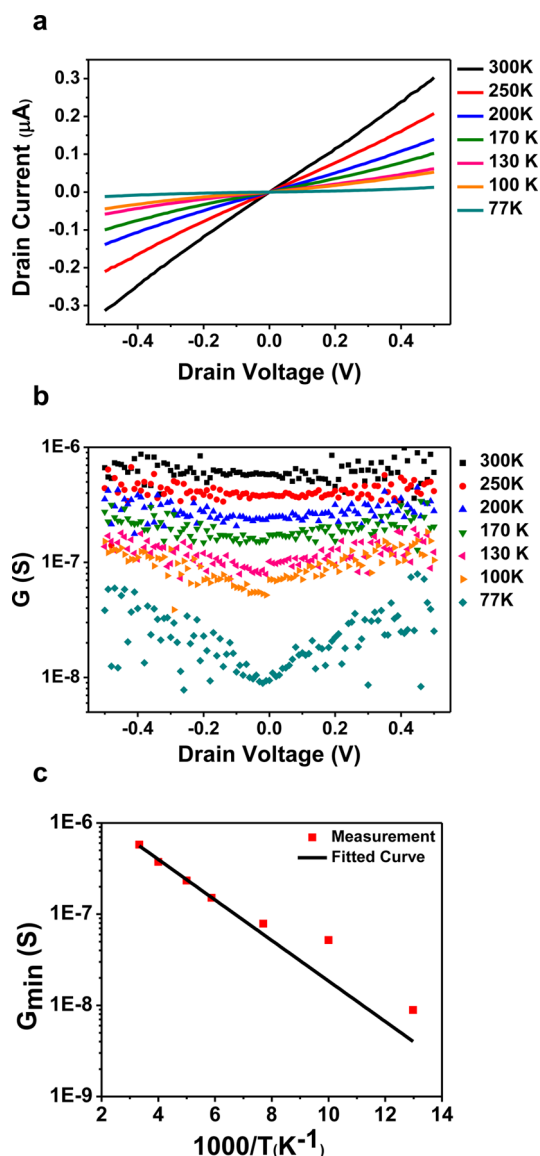


Figure 4. Temperature-dependent electrical measurements of 5 nm wide and 200 nm long GNR array: (a) output characteristics of the device under different temperatures; (b) minimum differential conductance ( $G_{\min}$ ) variation versus drain voltage at different temperatures; (c) minimum conductance vs inverse temperature and the corresponding curve fitting. The gate voltage was 0 V.

bandgap opening may provide higher sensitivity and a larger range of modulation of the electronic structure of the GNR compared with gapless graphene. In light of this motivation, we have performed gas sensing experiments using a 5 nm half-pitch HIBL GNR array with 200 nm channel length. The target gas we used in the experiments was nitrogen dioxide ( $\text{NO}_2$ ). High sensitivity to  $\text{NO}_2$  is very important for health and environmental safety as concentrations above 0.2 ppm can cause respiratory irritation.<sup>72</sup> Figure 5a shows the changes of the  $I_D$ – $V_d$  curves as a function of  $\text{NO}_2$  concentrations. Nitrogen was used as a dilution gas to obtain  $\text{NO}_2$  with different concentrations. It can be seen from Figure 5a that concentrations down to 20 ppb can

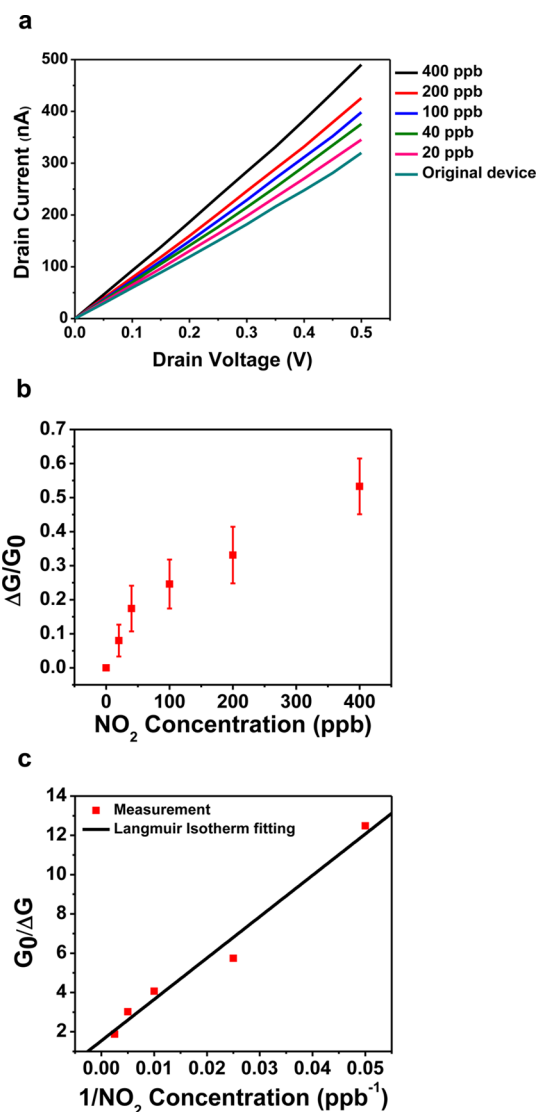


Figure 5. GNR array based  $\text{NO}_2$  gas sensor: (a) output characteristics of the GNR array sensor as a function of  $\text{NO}_2$  gas concentrations; (b) conductance change ( $\Delta G/G_0$ ) of the same GNR array sensor as a function of  $\text{NO}_2$  gas concentration. Error bars are extracted from the control experiment of the same device with Nitrogen flow only. (c) Langmuir isotherm curve fitting for the same device showing agreement between measured conductance values (red squares) and fitted curve (black line).

be clearly detected with the GNR array device. The GNR array FETs exhibit ambipolar transport behavior, as can be discerned from Figure 4. Since  $\text{NO}_2$  act as an electron acceptor, consequently, the GNR devices exhibit increased conductance with increasing the concentrations of  $\text{NO}_2$ . As control experiments, after finishing the  $\text{NO}_2$  sensing experiment and recovering the device back to the original conductance; the device was subjected to pure nitrogen environment to study the drift of the device conductance over time (Figure 3s). This step is aimed to rule out the time drift of the conductance of the device as a source of false signal. Figure 5b is showing conductance change  $\Delta G/G_0$  of  $\text{NO}_2$  sensing experiment. The sensor response

is defined as:

$$\frac{\Delta G}{G_0} = \frac{G_S - G_0}{G_0}$$

where  $G_0$  and  $G_S$  are the conductance of the device before gas exposure and after 1000 s of exposure to certain concentration of gas. The apparent difference in  $\Delta G/G_0$  between the sensing and control experiments indicates the sensitivity of the GNR array device to  $\text{NO}_2$  (Figures 5b and S4). Moreover, the measurement fits with the Langmuir isotherm for molecules absorbed on a surface. This indicates that charge transfer and monolayer molecular adsorption *via* site-binding govern the sensing mechanisms of the HIBL GNR array devices. Our device showed an unprecedented sensitivity for GNR FET based gas sensors. Novoselov *et al.*<sup>55</sup> have demonstrated single molecule sensitivity with a hall measurement system while a relatively small (4%) change of graphene device conductance was observed when exposed to 1 ppm  $\text{NO}_2$ . Also, other graphene based sensors showed even less  $\text{NO}_2$  sensitivity.<sup>57</sup> Comparatively, we observe a  $53 \pm 8\%$  change in conductance for 0.4 ppm concentration of  $\text{NO}_2$  gas. The high sensitivity of HIBL GNR array devices can be attributed to: (i) edge states of GNR which are more active sites for binding with  $\text{NO}_2$  gas molecules than pristine  $\text{sp}^2$  bonded

graphene surface,<sup>73</sup> (ii) the transition from a semimetal to a semiconductor after HIBL resulting in a reduced charge density and better current modulation by  $\text{NO}_2$  molecules. As previously mentioned, the charge traps in  $\text{SiO}_2$  may screen the gate electric field and negatively impact the transconductance; however, chemical sensing involves modulation of carrier density in GNR by electron extraction using  $\text{NO}_2$  and is not affected by charge traps inside  $\text{SiO}_2$ . This demonstrates the potential for using HIBL GNR arrays for high sensitive sensing applications.

## CONCLUSIONS

In summary, we developed an efficient method for patterning CVD grown graphene into narrow and tunable widths, highly aligned, densely packed and high aspect ratio GNR arrays using HIBL. Moreover, Raman spectra of HIBL GNR showed the relative high quality of the patterning and the resultant material. Additionally, we have revealed the existence of activation energy of 44 meV in carrier transport through the graphene/GNR junction. Finally, we showed the exceptional  $\text{NO}_2$  sensing performance of the GNR array device. The GNR array based sensor exceeded the performance of other graphene based sensors and is sensitive to low  $\text{NO}_2$  concentrations down to 20 ppb.

## METHODS

**Graphene Growth and Transfer.** Graphene was grown using a low pressure CVD growth on a 25  $\mu\text{m}$  thick copper foil (99.98% in purity). The copper foil was annealed at 1000  $^\circ\text{C}$  in hydrogen for 20 min. For graphene growth, temperature was maintained at 1000  $^\circ\text{C}$  for 30 min and a mixture of hydrogen, argon, and methane with flow rates of 4, 46, and 7 SCCM, respectively, was flowed at a pressure of 500 mTorr. Transfer was done by spin coating (2000 rpm, 1 min) two layers of methyl methacrylate (MMA) as a polymer scaffold on graphene and subsequently baking at 180  $^\circ\text{C}$  for 1 min to solidify the film and improve the adhesion. Afterward, copper was etched using a water diluted ferric chloride solution and the MMA/graphene film was rinsed with water and cleaned in a water diluted hydrochloric solution. The film was then transferred to the target substrate and MMA was removed using acetone and hydrogen annealing (350  $^\circ\text{C}$  and 2 h) subsequently.

**Helium Ion Beam Lithography.** The GNRs were patterned by direct helium ion beam milling using a helium ion microscope (Orion plus, Carl Zeiss SMT GmbH). The patterning was done using 5  $\mu\text{m}$  aperture size and a beam spot 4, which exhibited a 0.9 pA beam current. The patterns were written as single pixel lines with step size of about 0.3 nm. The dose to pattern 5 nm half-pitch GNRs was 10 nC/cm and larger doses were used to patterns with larger features.

**$\text{NO}_2$  Gas Sensing.** Gas sensing was carried out by exposing the GNR array FET device to nitrogen diluted  $\text{NO}_2$  gas in a closed chamber. Concentrations of  $\text{NO}_2$  were adjusted by changing the flow rates of both gases while keeping the total flow rate constant. For each curve, the device was exposed to the desired concentration for 1000 s and then the  $I_D-V_d$  curve was measured. Control device was subjected to the same measurement conditions (*i.e.*, same time between measurements and total flow rate) but with nitrogen gas only.

**Helium Ion Scattering Simulation.** Simulation was performed using a commercial program (SRIM). Simulation parameters

were as follows: helium ions, 1000 data points, 30 KeV energy and  $\text{SiO}_2/\text{Si}$  of 56 and 500 nm thicknesses, respectively.

**Conflict of Interest:** The authors declare no competing financial interest.

**Acknowledgment.** We would like to thank HP laboratories for the use of helium ion microscope. We thank Professor Kang L. Wang and Stephen B. Cronin for help with some of the experiments. We acknowledge the office of Naval Research for financial support.

**Supporting Information Available:** Raman spectrum of monolayer graphene (Figure S1), Raman spectra of G- and D-bands peak position vs GNR width (Figure S2), simulation of helium ions scattering and their effect on substrates and device operations (Figure S3), gas sensing control experiment electrical measurement (Figure S4), transport characteristics of 15 nm HIBL GNRs and conductance vs GNR width (Figure S5). This material is available free of charge *via* the Internet at <http://pubs.acs.org>.

## REFERENCES AND NOTES

- Novoselov, K. S.; Geim, A. K.; Morozov, S. V.; Jiang, D.; Zhang, Y.; Dubonos, S. V.; Grigorieva, I. V.; Firsov, A. A. Electric Field Effect in Atomically Thin Carbon Films. *Science* **2004**, *306*, 666–669.
- Balandin, A. A. Thermal Properties of Graphene and Nanostructured Carbon Materials. *Nat. Mater.* **2011**, *10*, 569–581.
- Balandin, A. A.; Ghosh, S.; Bao, W.; Calizo, I.; Teweldebrhan, D.; Miao, F.; Lau, C. N. Superior Thermal Conductivity of Single-Layer Graphene. *Nano Lett.* **2008**, *8*, 902–907.
- Kim, K. S.; Zhao, Y.; Jang, H.; Lee, S. Y.; Kim, J. M.; Kim, K. S.; Ahn, J.-H.; Kim, P.; Choi, J.-Y.; Hong, B. H.; *et al.* Large-Scale Pattern Growth of Graphene Films for Stretchable Transparent Electrodes. *Nature* **2009**, *457*, 706–710.

5. Lee, C.; Wei, X.; Kysar, J. W.; Hone, J. Measurement of the Elastic Properties and Intrinsic Strength of Monolayer Graphene. *Science* **2008**, *321*, 385–388.
6. Yan, H.; Low, T.; Zhu, W.; Wu, Y.; Freitag, M.; Li, X.; Guinea, F.; Avouris, P.; Xia, F. Damping Pathways of Mid-infrared Plasmons in Graphene Nanostructures. *Nat. Photonics* **2013**, *7*, 394–399.
7. Emani, N. K.; Chung, T.-F.; Ni, X.; Kildishev, A. V.; Chen, Y. P.; Boltasseva, A. Electrically Tunable Damping of Plasmonic Resonances with Graphene. *Nano Lett.* **2012**, *12*, 5202–5206.
8. Gu, T.; Petrone, N.; McMillan, J. F.; van der Zande, A.; Yu, M.; Lo, G. Q.; Kwong, D. L.; Hone, J.; Wong, C. W. Regenerative Oscillation and Four-Wave Mixing in Graphene Optoelectronics. *Nat. Photonics* **2012**, *6*, 554–559.
9. Liao, L.; Lin, Y.-C.; Bao, M.; Cheng, R.; Bai, J.; Liu, Y.; Qu, Y.; Wang, K. L.; Huang, Y.; Duan, X.; *et al.* High-speed Graphene Transistors with a Self-Aligned Nanowire Gate. *Nature* **2010**, *467*, 305–308.
10. Badmaev, A.; Che, Y.; Li, Z.; Wang, C.; Zhou, C. Self-Aligned Fabrication of Graphene RF Transistors with T-Shaped Gate. *ACS Nano* **2012**, *6*, 3371–3376.
11. Lin, Y.-M.; Dimitrakopoulos, C.; Jenkins, K. A.; Farmer, D. B.; Chiu, H.-Y.; Grill, A.; Avouris, P. 100-GHz Transistors from Wafer-Scale Epitaxial Graphene. *Science* **2010**, *327*, 662.
12. Britnell, L.; Gorbachev, R. V.; Jalil, R.; Belle, B. D.; Schedin, F.; Mishchenko, A.; Georgiou, T.; Katsnelson, M. I.; Eaves, L.; Morozov, S. V.; *et al.* Field-Effect Tunneling Transistor Based on Vertical Graphene Heterostructures. *Science* **2012**, *335*, 947–950.
13. Yang, H.; Heo, J.; Park, S.; Song, H. J.; Seo, D. H.; Byun, K.-E.; Kim, P.; Yoo, I.; Chung, H.-J.; Kim, K.; *et al.* Graphene Barristor, a Triode Device with a Gate-Controlled Schottky Barrier. *Science* **2012**, *336*, 1140–1143.
14. Georgiou, T.; Jalil, R.; Belle, B. D.; Britnell, L.; Gorbachev, R. V.; Morozov, S. V.; Kim, Y.-J.; Gholinia, A.; Haigh, S. J.; Makarovskiy, O.; *et al.* Vertical Field-Effect Transistor Based on Graphene-WS<sub>2</sub> Heterostructures for Flexible and Transparent Electronics. *Nat. Nanotechnol.* **2012**, *8*, 100–103.
15. Zeng, C.; Song, E. B.; Wang, M.; Lee, S.; Torres, C. M.; Tang, J.; Weiller, B. H.; Wang, K. L. Vertical Graphene-Base Hot-Electron Transistor. *Nano Lett.* **2013**, *13*, 2370–2375.
16. Yu, W. J.; Li, Z.; Zhou, H.; Chen, Y.; Wang, Y.; Huang, Y.; Duan, X. Vertically Stacked Multi-Heterostructures of Layered Materials for Logic Transistors and Complementary Inverters. *Nat. Mater.* **2012**, *12*, 246–252.
17. Elias, D. C.; Nair, R. R.; Mohiuddin, T. M. G.; Morozov, S. V.; Blake, P.; Halsall, M. P.; Ferrari, A. C.; Boukhvalov, D. W.; Katsnelson, M. I.; Geim, A. K.; *et al.* Control of Graphene's Properties by Reversible Hydrogenation: Evidence for Graphane. *Science* **2009**, *323*, 610–613.
18. Balog, R.; Jorgensen, B.; Nilsson, L.; Andersen, M.; Rienks, E.; Bianchi, M.; Fanetti, M.; Laegsgaard, E.; Baraldi, A.; Lizzit, S.; *et al.* Bandgap Opening in Graphene Induced by Patterned Hydrogen Adsorption. *Nat. Mater.* **2010**, *9*, 315–319.
19. Chang, C.-K.; Kataria, S.; Kuo, C.-C.; Ganguly, A.; Wang, B.-Y.; Hwang, J.-Y.; Huang, K.-J.; Yang, W.-H.; Wang, S.-B.; Chuang, C.-H.; *et al.* Band Gap Engineering of Chemical Vapor Deposited Graphene by *in Situ* BN Doping. *ACS Nano* **2013**, *7*, 1333–1341.
20. Lui, C. H.; Li, Z.; Mak, K. F.; Cappelluti, E.; Heinz, T. F. Observation of an Electrically Tunable Band Gap in Trilayer Graphene. *Nat. Phys.* **2011**, *7*, 944–947.
21. Velasco, J.; Jing, L.; Bao, W.; Lee, Y.; Kratz, P.; Aji, V.; Bockrath, M.; Lau, C. N.; Varma, C.; Stillwell, R.; *et al.* Transport Spectroscopy of Symmetry-Broken Insulating States in Bilayer Graphene. *Nat. Nanotechnol.* **2012**, *7*, 156–160.
22. Zou, K.; Zhang, F.; Clapp, C.; MacDonald, A. H.; Zhu, J. Transport Studies of Dual-Gated ABC and ABA Trilayer Graphene: Band Gap Opening and Band Structure Tuning in Very Large Perpendicular Electric Fields. *Nano Lett.* **2013**, *13*, 369–373.
23. Nakaharai, S.; Iijima, T.; Ogawa, S.; Suzuki, S.; Li, S.-L.; Tsukagoshi, K.; Sato, S.; Yokoyama, N. Conduction Tuning of Graphene Based on Defect-Induced Localization. *ACS Nano* **2013**, *7*, 5694–5700.
24. Son, Y.-W.; Cohen, M. L.; Louie, S. G. Energy Gaps in Graphene Nanoribbons. *Phys. Rev. Lett.* **2006**, *97*, 216803.
25. Han, M. Y.; Å–zyilmaz, B.; Zhang, Y.; Kim, P. Energy Band-Gap Engineering of Graphene Nanoribbons. *Phys. Rev. Lett.* **2007**, *98*, 206805.
26. Pan, M.; Girão, E. C.; Jia, X.; Bhaviripudi, S.; Li, Q.; Kong, J.; Meunier, V.; Dresselhaus, M. S. Topographic and Spectroscopic Characterization of Electronic Edge States in CVD Grown Graphene Nanoribbons. *Nano Lett.* **2012**, *12*, 1928–1933.
27. Bai, J.; Duan, X.; Huang, Y. Rational Fabrication of Graphene Nanoribbons Using a Nanowire Etch Mask. *Nano Lett.* **2009**, *9*, 2083–2087.
28. Abramova, V.; Slesarev, A. S.; Tour, J. M. Meniscus-Mask Lithography for Narrow Graphene Nanoribbons. *ACS Nano* **2013**, *7*, 6894–6898.
29. Jiao, L.; Zhang, L.; Wang, X.; Diankov, G.; Dai, H. Narrow Graphene Nanoribbons from Carbon Nanotubes. *Nature* **2009**, *458*, 877–880.
30. Kosynkin, D. V.; Higginbotham, A. L.; Sinitskii, A.; Lomeda, J. R.; Dimiev, A.; Price, B. K.; Tour, J. M. Longitudinal Unzipping of Carbon Nanotubes to Form Graphene Nanoribbons. *Nature* **2009**, *458*, 872–876.
31. Wei, D.; Xie, L.; Lee, K. K.; Hu, Z.; Tan, S.; Chen, W.; Sow, C. H.; Chen, K.; Liu, Y.; Wee, A. T. S. Controllable Unzipping for Intramolecular Junctions of Graphene Nanoribbons and Single-Walled Carbon Nanotubes. *Nat. Commun.* **2013**, *4*, 1374.
32. Xie, L.; Wang, H.; Jin, C.; Wang, X.; Jiao, L.; Suenaga, K.; Dai, H. Graphene Nanoribbons from Unzipped Carbon Nanotubes: Atomic Structures, Raman Spectroscopy, and Electrical Properties. *J. Am. Chem. Soc.* **2011**, *133*, 10394–10397.
33. Jiao, L.; Zhang, L.; Ding, L.; Liu, J.; Dai, H. Aligned Graphene Nanoribbons and Crossbars from Unzipped Carbon Nanotubes. *Nano Res.* **2010**, *3*, 387–394.
34. Wang, X.; Dai, H. Etching and Narrowing of Graphene from the Edges. *Nat. Chem.* **2010**, *2*, 661–665.
35. Wang, X.; Ouyang, Y.; Li, X.; Wang, H.; Guo, J.; Dai, H. Room-Temperature All-Semiconducting Sub-10-nm Graphene Nanoribbon Field-Effect Transistors. *Phys. Rev. Lett.* **2008**, *100*, 206803.
36. Li, X.; Wang, X.; Zhang, L.; Lee, S.; Dai, H. Chemically Derived, Ultrasoft Graphene Nanoribbon Semiconductors. *Science* **2008**, *319*, 1229–1232.
37. Cai, J.; Ruffieux, P.; Jaafar, R.; Bieri, M.; Braun, T.; Blankenburg, S.; Muoth, M.; Seitsonen, A. P.; Saleh, M.; Feng, X.; *et al.* Atomically Precise Bottom-Up Fabrication of Graphene Nanoribbons. *Nature* **2010**, *466*, 470–473.
38. Ruffieux, P.; Cai, J.; Plumb, N. C.; Patthey, L.; Prezzi, D.; Ferretti, A.; Molinari, E.; Feng, X.; Mullen, K.; Pignedoli, C. A.; *et al.* Electronic Structure of Atomically Precise Graphene Nanoribbons. *ACS Nano* **2012**, *6*, 6930–6935.
39. Schwab, M. G.; Narita, A.; Hernandez, Y.; Balandina, T.; Mali, K. S.; De Feyter, S.; Feng, X.; Mullen, K. Structurally Defined Graphene Nanoribbons with High Lateral Extension. *J. Am. Chem. Soc.* **2012**, *134*, 18169–18172.
40. Liang, X.; Wi, S. Transport Characteristics of Multichannel Transistors Made from Densely Aligned Sub-10 nm Half-Pitch Graphene Nanoribbons. *ACS Nano* **2012**, *6*, 9700–9710.
41. Kato, T.; Hatakeyama, R. Site- and Alignment-Controlled Growth of Graphene Nanoribbons from Nickel Nanobars. *Nat. Nanotechnol.* **2012**, *7*, 651–656.
42. Sokolov, A. N.; Yap, F. L.; Liu, N.; Kim, K.; Ci, L.; Johnson, O. B.; Wang, H.; Vosgueritchian, M.; Koh, A. L.; Chen, J.; *et al.* Direct Growth of Aligned Graphitic Nanoribbons from a DNA Template by Chemical Vapour Deposition. *Nat. Commun.* **2013**, *4*, No. 2402.
43. Solís-Fernández, P.; Yoshida, K.; Ogawa, Y.; Tsuji, M.; Ago, H. Dense Arrays of Highly Aligned Graphene Nanoribbons Produced by Substrate-Controlled Metal-Assisted Etching of Graphene. *Adv. Mater.* **2013**, *25*, 6562–6568.



44. Son, J. G.; Son, M.; Moon, K.-J.; Lee, B. H.; Myoung, J.-M.; Strano, M. S.; Ham, M.-H.; Ross, C. A. Sub-10 nm Graphene Nanoribbon Array Field-Effect Transistors Fabricated by Block Copolymer Lithography. *Adv. Mater.* **2013**, *25*, 4723–4728.
45. Pan, Z.; Liu, N.; Fu, L.; Liu, Z. Wrinkle Engineering: A New Approach to Massive Graphene Nanoribbon Arrays. *J. Am. Chem. Soc.* **2011**, *133*, 17578–17581.
46. Wang, X.; Ouyang, Y.; Jiao, L.; Wang, H.; Xie, L.; Wu, J.; Guo, J.; Dai, H. Graphene Nanoribbons with Smooth Edges Behave as Quantum Wires. *Nat. Nanotechnol.* **2011**, *6*, 563–567.
47. Koch, M.; Ample, F.; Joachim, C.; Grill, L. Voltage-Dependent Conductance of a Single Graphene Nanoribbon. *Nat. Nanotechnol.* **2012**, *7*, 713–717.
48. Sidorkin, V.; van Veldhoven, E.; van der Drift, E.; Alkemade, P.; Salemink, H.; Maas, D. Sub-10-nm Nanolithography with a Scanning Helium Beam. *J. Vac. Sci. Technol., B: Microelectron. Nanometer Struct.—Process., Meas., Phenom.* **2009**, *27*, L18–L20.
49. Winston, D.; Cord, B. M.; Ming, B.; Bell, D. C.; DiNatale, W. F.; Stern, L. A.; Vladar, A. E.; Postek, M. T.; Mondol, M. K.; Yang, J. K. W.; *et al.* In Scanning-Helium-Ion-Beam Lithography with Hydrogen Silsesquioxane Resist. *J. Vac. Sci. Technol., B: Microelectron. Nanometer Struct.* **2009**, *27*, 2702–2706.
50. Ward, B. W.; Notte, J. A.; Economou, N. P. In Helium Ion Microscope: A New Tool for Nanoscale Microscopy and Metrology. *J. Vac. Sci. Technol., B: Microelectron. Nanometer Struct.—Process., Meas., Phenom.* **2006**, *24*, 2871–2874.
51. Li, W.-D.; Wu, W.; Williams, R. S. Combined Helium Ion Beam and Nanoimprint Lithography Attains 4 nm Half-Pitch Dense Patterns. *J. Vac. Sci. Technol., B: Microelectron. Nanometer Struct.—Process., Meas., Phenom* **2012**, *30*, No. 06F304-4.
52. Lemme, M. C.; Bell, D. C.; Williams, J. R.; Stern, L. A.; Baugher, B. W. H.; Jarillo-Herrero, P.; Marcus, C. M. Etching of Graphene Devices with a Helium Ion Beam. *ACS Nano* **2009**, *3*, 2674–2676.
53. Bell, D. C.; Lemme, M. C.; Stern, L. A.; Williams, J. R.; Marcus, C. M. Precision Cutting and Patterning of Graphene with Helium Ions. *Nanotechnology* **2009**, *20*, 455301.
54. Ryu, S.; Maultzsch, J.; Han, M. Y.; Kim, P.; Brus, L. E. Raman Spectroscopy of Lithographically Patterned Graphene Nanoribbons. *ACS Nano* **2011**, *5*, 4123–4130.
55. Schedin, F.; Geim, A. K.; Morozov, S. V.; Hill, E. W.; Blake, P.; Katsnelson, M. I.; Novoselov, K. S. Detection of Individual Gas Molecules Adsorbed on Graphene. *Nat. Mater.* **2007**, *6*, 652–655.
56. Fowler, J. D.; Allen, M. J.; Tung, V. C.; Yang, Y.; Kaner, R. B.; Weiller, B. H. Practical Chemical Sensors from Chemically Derived Graphene. *ACS Nano* **2009**, *3*, 301–306.
57. Pearce, R.; Iakimov, T.; Andersson, M.; Hultman, L.; Spetz, A. L.; Yakimova, R. Epitaxially Grown Graphene Based Gas Sensors for Ultra Sensitive NO<sub>2</sub> Detection. *Sens. Actuators, B* **2011**, *155*, 451–455.
58. Reina, A.; Jia, X.; Ho, J.; Nezich, D.; Son, H.; Bulovic, V.; Dresselhaus, M. S.; Kong, J. Large Area, Few-Layer Graphene Films on Arbitrary Substrates by Chemical Vapor Deposition. *Nano Lett.* **2008**, *9*, 30–35.
59. Li, X.; Cai, W.; An, J.; Kim, S.; Nah, J.; Yang, D.; Piner, R.; Velamakanni, A.; Jung, I.; Tutuc, E.; *et al.* Large-Area Synthesis of High-Quality and Uniform Graphene Films on Copper Foils. *Science* **2009**, *324*, 1312–1314.
60. Ferrari, A. C.; Robertson, J. Interpretation of Raman spectra of Disordered and Amorphous Carbon. *Phys. Rev. B* **2000**, *61*, 14095–14107.
61. Gillen, R.; Mohr, M.; Thomsen, C.; Maultzsch, J. Vibrational Properties of Graphene Nanoribbons by First-Principles Calculations. *Phys. Rev. B* **2009**, *80*, 155418.
62. Ferrari, A. C.; Meyer, J. C.; Scardaci, V.; Casiraghi, C.; Lazzeri, M.; Mauri, F.; Piscanec, S.; Jiang, D.; Novoselov, K. S.; Roth, S.; *et al.* Raman Spectrum of Graphene and Graphene Layers. *Phys. Rev. Lett.* **2006**, *97*, 187401.
63. Banhart, F.; Kotakoski, J.; Krashenninnikov, A. V. Structural Defects in Graphene. *ACS Nano* **2010**, *5*, 26–41.
64. Duplock, E. J.; Scheffler, M.; Lindan, P. J. D. Hallmark of Perfect Graphene. *Phys. Rev. Lett.* **2004**, *92*, 225502.
65. Chen, Z.; Lin, Y.-M.; Rooks, M. J.; Avouris, P. Graphene Nanoribbon Electronics. *Phys. E* **2007**, *40*, 228–232.
66. Yinxiao, Y.; Murali, R. Impact of Size Effect on Graphene Nanoribbon Transport. *IEEE Electron Device Lett.* **2010**, *31*, 237–239.
67. Raza, H.; Kan, E. C. Armchair Graphene Nanoribbons: Electronic Structure and Electric-Field Modulation. *Phys. Rev. B* **2008**, *77*, 245434.
68. Hwang, Y.; Engel-Herbert, R.; Rudawski, N. G.; Stemmer, S. Effect of Postdeposition Anneals on the Fermi Level Response of HfO<sub>2</sub>/In<sub>0.53</sub>Ga<sub>0.47</sub>As Gate Stacks. *J. Appl. Phys.* **2010**, *108*, 034111.
69. Lin, H. C.; Brammertz, G.; Martens, K.; de Valicourt, G.; Negre, L.; Wang, W.-E.; Tsai, W.; Meuris, M.; Heyns, M. The Fermi-Level Efficiency Method and Its Applications on High Interface Trap Density Oxide-Semiconductor Interfaces. *Appl. Phys. Lett.* **2009**, *94*, No. 153508-3.
70. Bao, W.; Liu, G.; Zhao, Z.; Zhang, H.; Yan, D.; Deshpande, A.; LeRoy, B.; Lau, C. Lithography-Free Fabrication of High Quality Substrate-Supported and Freestanding Graphene Devices. *Nano Res.* **2010**, *3*, 98–102.
71. Huang, B.; Li, Z.; Liu, Z.; Zhou, G.; Hao, S.; Wu, J.; Gu, B.-L.; Duan, W. Adsorption of Gas Molecules on Graphene Nanoribbons and Its Implication for Nanoscale Molecule Sensor. *J. Phys. Chem. C* **2008**, *112*, 13442–13446.
72. ACGIH, Threshold Limit Values (TLVs) and Biological Exposure Indices (BEIs) - Nitrogen Dioxide. **2012**.
73. Radovic, L. R.; Bockrath, B. On the Chemical Nature of Graphene Edges: Origin of Stability and Potential for Magnetism in Carbon Materials. *J. Am. Chem. Soc.* **2005**, *127*, 5917–5927.